J. Am. Soc. Mass Spectrom. (2019) 30:2068–2081
DOI: 10.1007/s13361-019-02275-7

RESEARCH ARTICLE

Weak Acid-Base Interactions of Histidine and Cysteine Affect the Charge States, Tertiary Structure, and Zn(II)-Binding of Heptapeptides

Yu-Fu Lin, Enas N. Yousef, Efren Torres, Linh Truong, James M. Zahnow, Cole B. Donald, Ying Qin, Laurence A. Angel

Department of Chemistry, Texas A&M University-Commerce, 2600 S Neal St, Commerce, TX 75428, USA

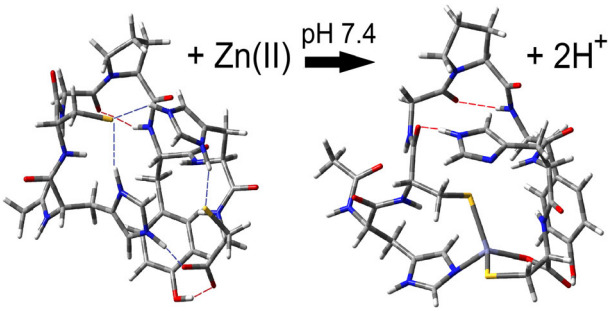

Abstract. Zinc fingers are proteins that are characterized by the coordination of zinc ions by an amino acid sequence that commonly contains two histidines and two cysteines (2His-2Cys motif). Investigations of oligopeptides that contain the 2His-2Cys motif, e.g., acetyl-His_1-Cys_2-Gly_3-Pro_4-Tyr_5-His_6-Cys_7, have discovered they exhibit pH-dependent Zn(II) chelation and have redox activities with Cu(I/II), forming a variety of metal complexes. To further understand how these 2His-2Cys oligopeptides bind these metal ions, we have undertaken a series of ion mobility–mass spectrometry and B3LYP/LanL2DZ computational studies of structurally related heptapeptides. Starting with the sequence above, we have modified the potential His, Cys, or C-terminus binding sites and report how these changes in primary structure affect the oligopeptides positive and negative charge states, conformational structure, collision-induced breakdown energies, and how effectively Zn(II) binds to these sequences. The results show evidence that the weak acid-base properties of Cys-His are intrinsically linked and can result in an intramolecular salt-bridged network that affects the oligopeptide properties.

Keywords: 2His-2Cys motif, Peptide tertiary structure, Histidine charge state, Cysteine charge state, Salt-bridge, B3LYP/LanL2DZ, Ion size scaled Lennard-Jones, Collision cross-sections

Received: 17 February 2019/Revised: 10 June 2019/Accepted: 18 June 2019/Published Online: 22 July 2019

Introduction

Predicting the higher order structure of oligopeptides and metallopeptides based on their primary structure is an important component for understanding protein folding and a key step in designing bioactive peptides or proteins. NMR spectroscopy and X-ray crystallography are the most commonly used techniques for providing atomic resolution of peptides or proteins' secondary/tertiary structure. For NMR, the conformational interpretation is not straightforward for flexible oligopeptides and when multiple species are present [1]. Moreover, X-ray diffraction studies of metallopeptides are scarce due to problems with the crystallization of these complexes [2]. An alternative technique is electrospray ionization–ion mobility–mass spectrometry (ESI-IM-MS), which can quantify the populations of metallopeptides and infer intramolecular interactions after the evaporation of the solvent [3–7]. A recent study showed how Cu(I/II)-bound peptides that only differed by their number of inter- or intramolecular disulfide bridges, number of Cu(I) or Cu(II) ions, and their deprotonation sites could be resolved by ESI-IM-MS [8]. Native ESI-IM-MS uses soft ESI conditions and transmission parameters to try to preserve the solution-phase populations, conformations, and noncovalent interactions and was used to determine the populations and conformational states of Zn(II)-bound peptides derived from histidine-rich glycoprotein [9]. Over the last

Electronic supplementary material The online version of this article (https://doi.org/10.1007/s13361-019-02275-7) contains supplementary material, which is available to authorized users.

Correspondence to: Laurence Angel; *e-mail:* Laurence.Angel@tamuc.edu

7 years, our lab has undertaken ESI-IM-MS studies of the methanobactin [10, 11] from *Methylosinus trichosporium* (mb-OB3b) and a series of analog methanobactin (amb) oligopeptides [8, 12–14]. Methanobactins [15] are Cu(I)-binding oligopeptides secreted by methanotrophic bacteria in response to copper availability in their growth environment [16, 17]. The primary structure of mb-OB3b contains two oxazolone rings associated with enethiols and separated by 4 amino acids and pyrrolidine [18]. X-ray crystallography has shown that Cu(I) is coordinated by a distorted tetrahedral geometry by the two enethiol-oxazolones [19]. The amb oligopeptides were designed with sequences that mimicked the primary sequence of mb-OB3b but replaced the two enethiol-oxazolone ligands with two His-Cys ligands (2His-2Cys motif) used by zinc fingers to selectively coordinate Zn(II) [20]. The studies showed that mb-OB3b and the ambs exhibited pH-dependent reactivity that could be closely correlated to that of the solution phase and further showed ESI-IM-MS as a powerful analytical technique for characterizing peptide interactions with metal ions.

Here, we have undertaken a new series of ESI-IM-MS and DFT studies to interrogate the effect of the 2His-2Cys motif on the charge states, tertiary structure and Zn(II)-binding of six new amb oligopeptides (Scheme 1). [12, 13] The charge states of these ambs will be affected by the gas-phase basicities [21] of the 2His and the Pro residues [22, 23] and the gas-phase acidities [24] of the carboxyl group at the C-terminus and the substituent groups of the 2Cys and Tyr. Coulomb repulsion between two positive charge sites can also affect their apparent gas-phase basicities and the conformational structure of the oligopeptide [25–27]. Solvent composition [28] and droplet desolvation during ESI [29] also affects the charge of the peptide. Previous work has shown a disparity between the positive charge state distributions of oligopeptides produced from ESI to those of solution-phase equilibria [30]. Considering pK_as and solution-phase chemistry, the hexaprotic ac-His_1-Cys_2-Gly_3-Pro_4-Tyr_5-His_6-Cys_7 (Scheme 1A) would exhibit an overall charge state based on the protonation state of the carboxyl group at the C-terminus (pKa ≈ 3) [31], 2His (pKa ≈ 6.0) [32, 33], 2Cys (pKa < 8.3) [34], and Tyr (pKa ≈ 11.0), and generally form positively charged ions at pH < 6.0 and negatively charged ions at pH > 6.0.

The energy-resolved collision-induced dissociation (CID) of peptides is used for protein identification in proteomics [35] and more fundamentally has been applied with molecular modeling to understand the structure of ions and mechanisms of peptide fragmentation [36–39]. Studies of small peptides include the formation and fragmentation mechanisms of Zn(II) complexes of Gly [40–42]; transition metal-bound polyalanines [43]; metal-binding sites of angiotensin I [7]; Pd(II) sites of ubiquitin [44]; peptides that contain His [9, 45, 46], Cys [47–49], Pro [50, 51], Phe [52, 53], Met [49, 54], Arg [55], Lys [46], and Gly; [56, 57]; and the structures of ***a*** [58] and ***b*** ions. [59, 60] The salt-bridges in the tertiary structure of small proteins have also been investigated by CID in combination with electron transfer dissociation [61].

Previously, our study of amb_{5A} (Scheme 1A) and its amidated C-terminus counterpart **B** indicated that these peptides can bind Zn(II) via different charge state conformers including coordination by the 2His-2Cys, backbone carbonyl groups, and C-terminus. [14] Zinc(II) is an essential cofactor involved in many metabolic enzymes and transcription factors, preferring "softer" ligands such as Cys and His [20]. For example, in metabolic enzymes, Zn(II) is partially exposed to the solvent and is found tetrahedrally coordinated via 3His and a water molecule in carbonic anhydrase, while other enzymes utilize Cys, Asp, or Glu. For transcription factors such as the Zn-finger family, Zn(II) is most commonly found tetrahedrally coordinated via the 2His-2Cys motif, although His-3Cys and 4Cys are also binding motifs [20].

For this endeavor, the series of heptapeptides **A** to **G** (Scheme 1) have been chosen to test whether their differences in overall charge state, tertiary structure, and Zn(II) chelation can be attributed to the His, Cys, or C-terminus sites. Scheme 1 shows the structure of the "parent" sequence **A**, and the modifications to that sequence, e.g., amidation of the C-terminus (**B**), replacement of His_6 by Gly_6 (**C**), replacement of His_1 and His_6 by Gly_1 and Gly_6 (**D**), replacement of Cys_2 by Gly_2 (**E**), replacement of Cys_2 and Cys_7 by Gly_2 and Gly_7 (**F**), and replacement of His_1 and His_6 by Cys_1 and Cys_6 and amidation of the C-terminus (**G**).

Experimental Section

Reagents and Sample Preparation

The design of the heptapeptides were based on incorporating features from zinc fingers, i.e., the 2His-2Cys motif, the symmetric N- and C-terminal arms connected via the tight turn of the Pro, with the Tyr residue providing a possible π-cation interaction between the aromatic ring and the zinc ion. The heptapeptides **A** and **B** were synthesized by Neo BioLab (https://neobiolab.com) and **C**, **D**, **E**, **F**, and **G** by PepmicCo (http://www.pepmic.com/). Ammonium hydroxide (trace metal grade) and glacial acetic acid (Optima grade) were both purchased from Fisher Scientific (http://www.Fishersci.com), and $ZnCl_2$ (98 + %) and $Zn(NO_3)_2{\cdot}6H_2O$ (99%) were purchased from Alfa Aesar (http://www.alfa.com). Solutions of 25.0 μM **A** to **G** or molar equivalents **A** to **G** and Zn(II) were prepared with > 17.8 MΩ cm deionized (DI) water (http://www.millipore.com), pH adjusted with glacial acetic acid or ammonium hydroxide and left to stand for 10 min before IM-MS analysis and pH measurement using a calibrated Orion 98 micro pH electrode. Experiments were repeated using $ZnCl_2$ and $Zn(NO_3)_2{\cdot}6H_2O$ to check for reproducibility and estimate the standard deviations. The collision cross section calibrant poly-DL-alanine was purchased from Sigma-Aldrich (http://www.sigmaaldrich.com) and dissolved in DI water/acetonitrile (50/50) to a final concentration of 10 ppm as previously described. [62, 63]

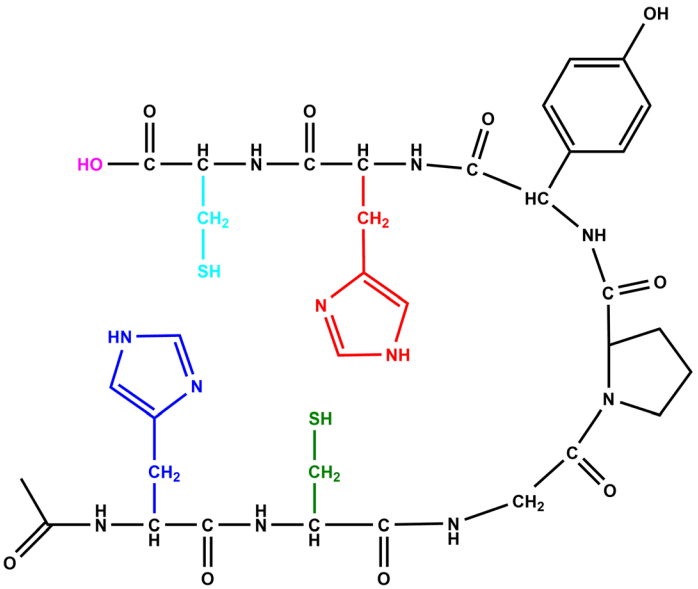

A ac-His_1-Cys_2-Gly_3-Pro_4-Tyr_5-His_6-Cys_7-OH
B ac-His_1-Cys_2-Gly_3-Pro_4-Tyr_5-His_6-Cys_7-NH_2
C ac-His_1-Cys_2-Gly_3-Pro_4-Tyr_5-Gly_6-Cys_7-OH
D ac-Gly_1-Cys_2-Gly_3-Pro_4-Tyr_5-Gly_6-Cys_7-OH
E ac-His_1-Gly_2-Gly_3-Pro_4-Tyr_5-His_6-Cys_7-OH
F ac-His_1-Gly_2-Gly_3-Pro_4-Tyr_5-His_6-Gly_7-OH
G ac-Cys_1-Cys_2-Gly_3-Pro_4-Tyr_5-Cys_6-Cys_7-NH_2

Scheme 1. The primary sequence of **A** (MW = 857.96 Da, p*I* = 6.03) where ac = acetyl group and the color highlighting the regions modified with bold underscore for **B** (MW = 856.96, p*I* = 7.09); **C** (MW = 777.87, p*I* = 2.06); **D** (MW = 697.78, p*I* < 2.0); **E** (MW = 811.87, p*I* = 6.03); **F** (MW = 765.77, p*I* = 6.04); and **G** (MW = 788.99, p*I* < 8.3). The p*I* was calculated using https://pepcalc.com/ apart from **D** and **G** which have no basic groups and their p*I* is shown as an upper level based on the pK_a of either the carboxylate C-terminus or Cys group, respectively

Waters Synapt High-Definition Mass Spectrometer (HDMS)

The samples were electrosprayed into a Waters Synapt High-Definition Mass Spectrometer (G1) [64] with a flow rate of 10 μL min^{-1} and 2.0-kV capillary voltage with the sampling cone 25 V and the extraction cone 3.0 V. Preliminary experiments showed that all ions appeared in the 50–2500 *m/z* region, and the quadrupole mass analyzer was used to guide all the ions to the three traveling wave (T-wave) ion guides or resolve the precursor ion for CID studies. The trap ion guide was operated with 4-V entrance voltage and a pressure of 2.25×10^{-2} mbar with an argon gas flow of 1.5 mL/min. The trap served as a storage cell for gating ions into the ion mobility (IM) T-wave ion guide. The IM ion guide was operated at a pressure of 0.518 mbar with a flow rate of 20.0 mL min^{-1} N_2 buffer gas with ramped T-wave heights of 7.5–16.4 V (+ ion mode) or 13.0–22.0 V (−) and ramped T-wave velocities of 600–1400 m s^{-1}, for every sweep of the IM T-wave ion guide. The transfer T-wave cell, with the same argon pressure as the trap, passed on the ion mobility separated ions to the orthogonal time-of-flight for *m/z* analysis, where the ion mobility–mass spectrum was acquired by synchronizing the gated release of ions into the mobility T-wave ion guide with the time-of-flight mass spectral acquisition.

Analysis of the $amb_{5A\text{-}G}$ IM-MS Spectra

The IM-MS analysis allowed for drift time separation and *m/z* identification of all the various amb_5 species including coincidental *m/z* species. The positively and negatively charged species were identified based on their *m/z* and isotope patterns, and their drift time distributions were extracted using Driftscope 2.0. The centroid of each drift time distribution and the area under the drift time curve was determined using MassLynx 4.1. The centroids of the drift time distributions were used to calculate the collision cross sections of the various amb_5 species, and the areas under the drift time curves were used to calculate their percent relative intensities at each pH step. The experiments were repeated 2–5 times to estimate the standard deviations.

Collision-Induced Dissociation and Breakdown Curves

To study the energy-dependent CID of **A** to **G**, the isotope distribution of the chosen precursor ions were resolved by the linear quadrupole, passed through the trap and the IM cells, and dissociated in the transfer T-wave cell using the lab-frame collision energy (CE) controlled by the entrance lens which resulted in reproducible breakdown curves [65]. The precursor and product ions were *m/z* analyzed by the TOF and identified by matching their isotope patterns to their theoretical isotope patterns from the MassLynx 4.1 software. The percent relative intensities of the precursor and product ions were calculated by normalizing their area under the drift time curve to the total area of all species produced at each CE.

Collision Cross Sections

Collision cross sections (CCSs) of the amb_5 species were measured using a calibration method that provides CCS as measured in He gas (Ω_{He}) and allowed us to compare the Ω_{He} with those calculated by the Sigma program. In this method, previously measured CCS of poly-DL-alanine (PA) for negative [63, 66] and positive ions [62] measured in He gas

(Ω_{He}) [67] were used to determine the Ω_{He} of the amb_5 species. The PA Ω_{He} were converted to corrected CCS (Ω_c) by Eq. (1), where z = charge of ion, $e_c = 1.602 \times 10^{-19}$ C, m_{N2} = mass of N_2 (Da), and m_{ion} = mass of the ion [68].

$$\Omega c = \frac{\Omega_{He}}{ze_c \sqrt{\left(\frac{1}{m_{N_2}} + \frac{1}{m_{ion}}\right)}} \quad (1)$$

From the IM-MS analyses, the centroid of the measured arrival times (t_A) for the calibrants and amb_5 species were converted to centroid IM drift times (t_D) using Eq. (2), where c = enhanced duty cycle delay coefficient (1.41).

$$t_D = t_A - \frac{c\sqrt{m/z}}{1000} \quad (2)$$

The t_D for the calibrants were plotted against their Ω_c and using a least-squares regression fit the A' and B constants were obtained using Eq. (3), where A' is the correction for the temperature, pressure, and electric field parameters and B compensates for the nonlinear effect of the IM device. Four separate calibration curves were constructed for the singly and doubly charged species from the negative and positive ion analyses.

$$\Omega_c = A' t_D{}^B \quad (3)$$

Using these A' and B values the t_D for the amb_5 species were converted to Ω_c using Eq. (3), and Ω_{He} using Eq. (1). The reported Ω_{He} are an average from 3 to 5 separate measurements and have estimated absolute errors of 2% [62, 63, 66].

Computational Methods

The B3LYP/LanL2DZ level of theory containing the Becke three parameter hybrid functionals with the Dunning basis set [69] and electron core potentials [70–72] from Gaussian 09 [73] was used to locate the geometry-optimized, gas-phase structures of species **A** to **G**. Optimization of gas-phase structures was chosen because our previous research on ac-His-Cys-Tyr-Pro-His-Cys (amb_2) and **A** showed the inclusion of the SMD aqueous model produced similar results as the gas-phase method [13, 14]. For each calculation, initial structures were made in GaussView 5 based on various possible interactions between the substituent sites of His, Cys, Tyr, and the C-terminus which resulted in the overall charge of the conformer, while keeping all the amide bonds in the peptide backbone in their *trans*-configuration including Pro_4. Optimized structures were modified using GaussView 5 to produce new starting structures for optimizations to further sample the conformational space of the conformers.

The CCSs were calculated for the geometry-optimized complexes using the ion size scaled Lennard-Jones (LJ) method from the Sigma program, developed and written by the Bowers group from the Department of Chemistry and Biochemistry at the University of California - Santa Barbara [74]. The LJ values are derived from the mean and standard deviation from 10 repeated calculations.

Results and Discussion

Positive Ion Charge Distributions of $amb_{5A\text{-}G}$ over pH 3 to pH 11

As discussed earlier, the hexaprotic amb_{5A} (Scheme 1A) should exhibit an overall charge state based on the protonation state of the 2His, 2Cys, Tyr, Pro, and carboxyl group of the C-terminus. The relative populations of the two observed charge states $[amb_{5A\text{-}G} + H]^+$ and $[amb_{5A\text{-}G} + 2H]^{2+}$ electrosprayed from pH 2.9 to pH 10.9 solutions are shown in Figure 1 a and b, respectively. At pH 2.9, the species with both His_1 and His_6 imidazolium groups in the primary structure, **A**, **B**, **E**, and **F**, exhibited 75–82% intensity of the 2+ charge state, $[amb_5 + 2H]^{2+}$, which decreased to 56–61% as pH increased to pH 4.7. For **A**, **E**, and **F**, the deprotonation of the C-terminus carboxyl group, which favorably deprotonates over this pH range, could explain the overall charge state decrease from 2+ to 1+. For **B**, the deprotonation of the His imidazolium or the C-terminus amide group [75] was needed to decrease the charge, with B3LYP/LanL2DZ predicting the deprotonation of His_1 was 29 kJ/mol more favorable than deprotonation of the C-terminus amide group (Figure S1). Above pH 4.7, the relative intensities of the 1+ and 2+ charge states did not change significantly, indicating that they were not influenced by solution-phase equilibria. For **C**, **D**, and **G**, the single-charged $[amb_5 + H]^+$ predominated over the whole pH 2.9 to 10.9 range because they either contained just one or zero imidazolium groups in their primary structure. For **C**, the remaining His_1 imidazolium could hold the 1+ charge, but for **D** or **G**, the 1+ charge site was likely either Pro_4, which exhibited the next highest gas-phase basicity after His [21–23] or solvation of the proton by carbonyl and/or thiol groups, with B3LYP predicting the solvation of the proton by two thiols was 14 kJ/mol less favorable in free energy than the protonation of Pro_4 (Figure S2).

Collision Cross Sections and Tertiary Structures of Positive Ions

The CCS as measured in helium gas (Ω_{He}) of the different charge states were measured by IM-MS (Table 1) and compared to the Ω_{He} of the low energy conformers located from the B3LYP/LanL2DZ method as calculated by the LJ method. For $[amb_{5A} + H]^+$, the three lowest energy B3LYP conformers differed by < 1 kJ/mol in free energy and all had *trans*-Pro_4 forming the hinge of the two arms, with the imidazolium group of His_1 salt-bridged to the carboxylate group of the C-terminus (SB-1 in Figure 1c) and 4 hydrogen bonds, including His_6 hydrogen bonded to backbone carbonyl groups and the hydroxyl group of Tyr_5 hydrogen bonded to the carboxylate of the C-terminal (H-1) or the acetyl group of the N-terminal. These intramolecular interactions resulted in folded conformers with

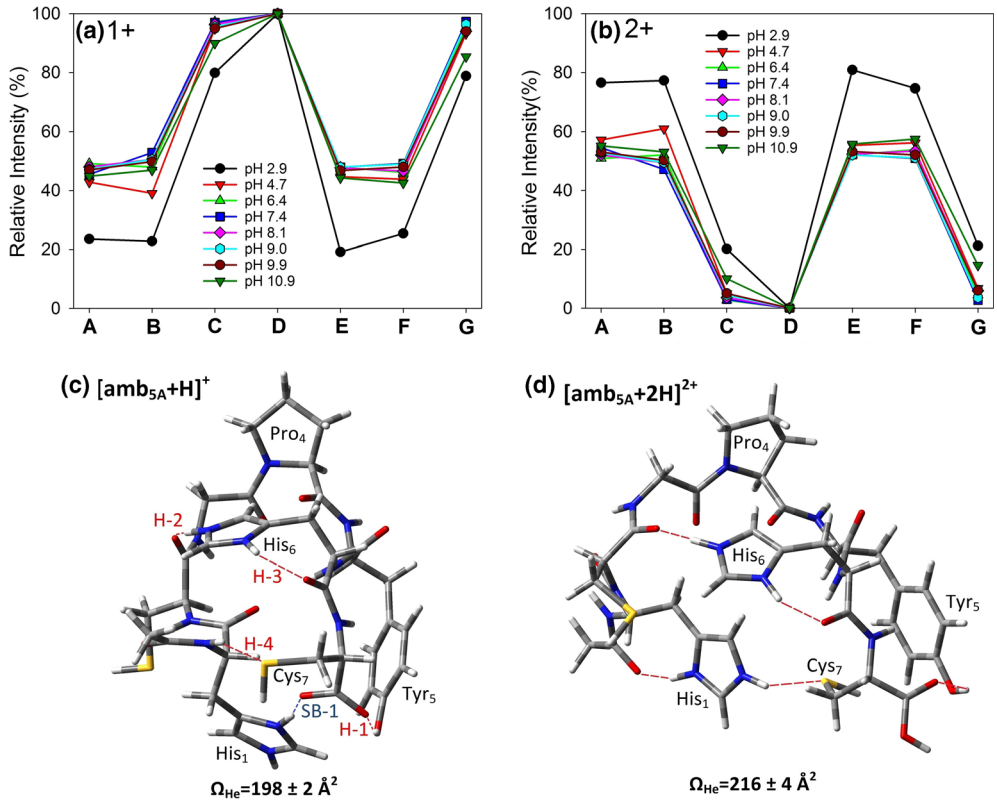

Figure 1. Relative intensities of the positive charge states of species **A** to **G**, (**a**) $[amb_5 + H]^+$ and (**b**) $[amb_5 + 2H]^{2+}$over the pH range of pH 2.9–10.9. The lowest free energy conformers located using the B3LYP/LanL2DZ method (**c**) $[amb_{5A} + H]^+$ and (**d**) $[amb_{5A} + 2H]^{2+}$ with their theoretical collision cross sections (Ω_{He}) measured by the ion size scaled Lennard-Jones method [74]. The dashed lines represent the salt-bridges (---) and hydrogen bonds (---) that stabilize their tertiary structures with labels referred to in the text

theoretical CCS (Ω_{He}) of 198 to 199 Å^2, which all agreed with the IM-MS measured $\Omega_{He} = 199 \pm 4$ Å^2 (Table 1). The lowest free energy conformer ($\Omega_{He} = 198 \pm 2$ Å^2, Figure 1c) included three hydrogen bonds from the substituents of His_6 (H-2, H-3) and Cys_7 (H-4) to backbone amide groups. These interactions were exhibited in the tertiary structures of other $[amb_5 + H]^+$ species (Figures S1 and S3) with theoretical Ω_{He} that also agreed with the experimentally measured IM-MS Ω_{He} in Table 1.

The two lowest free energy 2+ conformers of **A** located by B3LYP/LanL2DZ differed by only 14 kJ/mol, but they exhibited different CCS of $\Omega_{He} = 216 \pm 4$ Å^2 (Figure 1d) and 247 ± 3 Å^2 (Figure S4), with only the Ω_{He} of the former matching the IM-MS measured $\Omega_{He} = 216 \pm 2$ Å^2 (Table 1). This 2+ conformer **1d** exhibited four hydrogen bonds from the two imidazoliums to carbonyl or thiol groups and another hydrogen bond between Tyr_5 and the C-terminus which stabilized its overall conformation. The more extended conformer (Figure S4) also exhibited four hydrogen bonds and was predicted by B3LYP to be the lowest in free energy. This indicates that the B3LYP calculations should not be used alone, and comparison with the experimental IM-MS measured Ω_{He} is necessary. This is especially relevant as the ESI process might produce kinetically trapped species rather than the lowest energy structures. Also, there maybe more than just one conformer present as indicated by the three lowest energy 1+ conformers that differed by < 1 kJ/mol and had similar sized CCS and hydrogen-bonded structures. The CID results discussed later also support the selected conformers because the removal of the imidazolium groups, which are integral to

Table 1. Collision Cross Sections (Å^2) Measured in Helium (Ω_{He}) Buffer Gases for Positive and Negative Ions of amb_{5A-G} (H Loss or Gain Not Shown) by Ion Mobility–Mass Spectrometry with Estimated Absolute Uncertainties of ± 4 Å^2

amb_5	$[amb_5]^+$	$[amb_5]^{2+}$	$[amb_5]^-$	$[amb_5]^{2-}$	$[amb_5 + Zn]^+$	$[amb_5 + Zn]^{2+}$	$[amb_5 + Zn]^-$
A	199	216	196	218	205	217	200
B	201	213	201	214	208	213	203
C	190	208	182	197	191	205	188
D	173	–	168	190	177	186	170
E	192	208	189	213	191	207	194
F	186	203	179	202	182	199	180
G	189	191	210	204	196	200	190

these salt-bridged and hydrogen-bonded conformers, result in a substantial decrease of 20 eV (lab-frame) in their breakdown energies.

Negative Ion Charge Distributions of amb$_{5A-G}$ over pH 3 to pH 11

Comparison of the relative intensities of the 1- and 2- charged species (Figure 2a, b) showed the principal species was [amb$_5$ – H]$^-$ which decreased over pH 2.9–10.9 with [amb$_5$ – 2H]$^{2-}$ exhibiting the greatest increase (10–28%) between pH 9.9 and 10.9. The potential negative charge sites are the Cys, Tyr, or C-terminus, but it was the substitution of the 2His by 2Gly or 2Cys that most adversely affected the relative intensity of the 2- charge state as observed for **D** and **G**. At first, this seems counterintuitive because the removal of a positively charged imidazolium group may be expected to make the 2- charge state more probable. However, the pK_as of His and Cys bracket pH 7 by ± 1 unit and interactions between the weak imidazole bases and weak thiol acids can stabilize the negative charge of the deprotonated thiolates as demonstrated by the B3LYP modeling and CCS measurements described next.

Collision Cross Sections and Tertiary Structures of Negative Ions

The B3LYP conformer located for the 1- charge of **A** (Figure 2c) exhibited four salt-bridges between the imidazoliums of His$_1$ and His$_6$ and the thiolates of Cys$_2$, Cys$_7$, and carboxylate of the C-terminal. These salt-bridges were produced by the B3LYP geometry optimization even if the protons started on the thiol groups because the proton transfer to the imidazoles proceeded without an energy barrier. The stability contributed by these salt-bridges to the 1- conformer was also supported by the negative charge state distributions which showed the 1- charge state remained the predominant species over the pH 2.9–10.9 range. The lowest energy conformer **2c** included hydrogen bonds between the C-terminus and hydroxyl group of Tyr$_5$, and the backbone amide of Tyr$_5$ and carbonyl group of Pro$_4$ resulting in a folded structure with a theoretical Ω_{He} = 196 ± 2 Å^2 which matched the IM-MS measured Ω_{He} = 196 ± 4 Å^2 (Table 1). The next two lowest B3LYP conformers located had fewer salt-bridges of three and one, respectively, and higher free energies of 28 kJ/mol and 57 kJ/mol than **2c**. Salt-bridges were present in the tertiary structures of the lowest free energy conformers of **B** and **C** (Figure S5), whose LJ Ω_{He} were also in agreement with the IM-MS Ω_{He} measurements (Table 1). Unlike with the positive ions, the negative ion conformers had larger free energy differences between conformers and our approach of using B3LYP to locate conformers and compare them with the IM-MS measured CCS and charge state distributions revealed the significant stability of the intramolecular salt-bridge network for conformer **2c**. Moreover, the breakdown energies discussed later support the stability of the **2c** conformer.

The lowest free energy 2- conformer of **A** (Figure S6) was folded by hydrogen bonds between the imidazoles, thiol(ate), and carboxylate in a similar way to **2c**. However, this conformer's

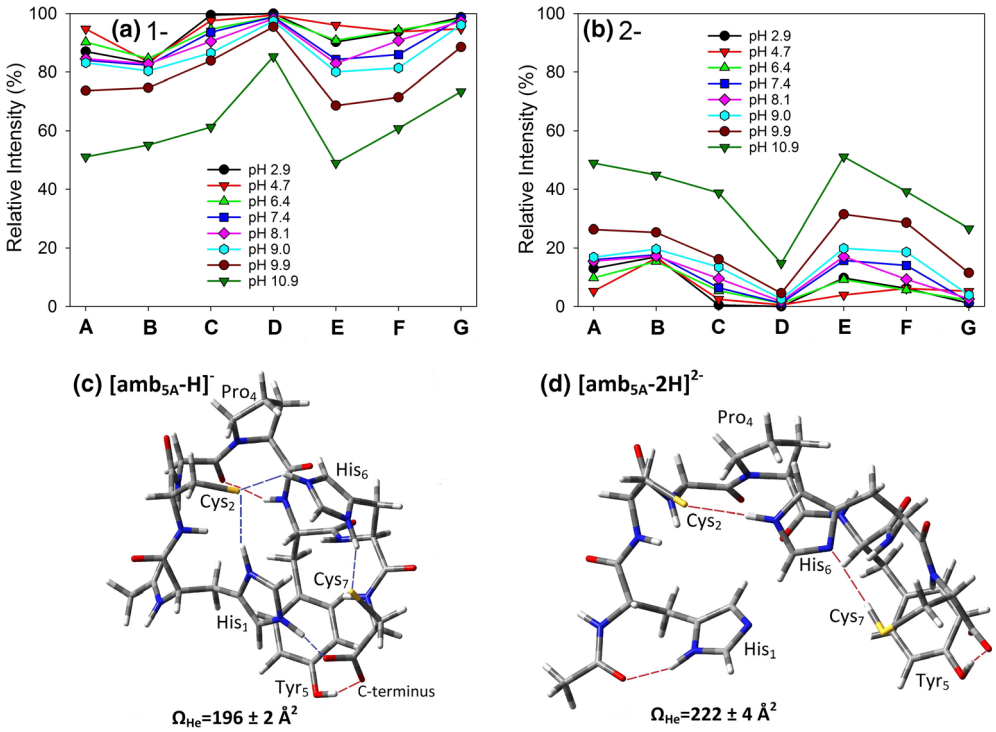

Figure 2. Relative intensities of the negative charge states of species **A** to **G**, (**a**) [amb$_5$ – H]$^-$ and (**b**) [amb$_5$ – 2H]$^{2-}$ over the pH range of pH 2.9–10.9. The lowest energy conformers located using the B3LYP/LanL2DZ method (**c**) [amb$_{5A}$ – H]$^-$ and (**d**) [amb$_{5A}$ – 2H]$^{2-}$ with theoretical collision cross sections (Ω_{He}) measured using the ion size scaled Lennard-Jones method [74]. The dashed lines represent the salt-bridges (- - -) and hydrogen bonds (- - -) that stabilize their tertiary structures

theoretical $\Omega_{He} = 195 \pm 2$ Å^2 was 23 Å^2 smaller than the IM-MS measured $\Omega_{He} = 218 \pm 2$ Å^2 (Table 1), which suggested a more open structure existed. A more extended structure 26 kJ/mol higher in free energy (Figure 2d) exhibited a tertiary structure with hydrogen bonding between the 2His, 2Cys, and acetylated N-terminus, with Tyr_5 also hydrogen bonded to the C-terminus. This conformer's LJ $\Omega_{He} = 222 \pm 4$ Å^2 was in good agreement with the IM-MS $\Omega_{He} = 218 \pm 2$ Å^2.

Collision-Induced Dissociation Studies and Breakdown Energies

The CID spectra of $[amb_{5A\text{-}G}]^+$ exhibited a series of ***a***, ***b***, and ***y***-type product ions [76], and **A**, **B**, **E**, and **F** exhibited the most similar CID spectra because they all contained the His_1 and His_6 residues (Figure S7). The **C** and **D** precursors differed by *not* producing the $\boldsymbol{y}_2$ ion (**C**), or the $\boldsymbol{y}_2$, $\boldsymbol{b}_2$, $\boldsymbol{b}_1$, and $\boldsymbol{a}_1$ ions (**D**), which only formed when the His_1 or His_6 were present, consistent with previous studies that showed the $\boldsymbol{b}_1$ ion formed if the N-terminal substituent group can transfer a proton to the N-terminal amine N and/or cleave the first amide bond via nucleophilic attack [45, 55]. When both His residues were replaced by Gly (**D**), most product ions contained the Pro_4 residue which supported that the enhanced gas-phase basicity of Pro_4 made it a favorable proton site after His [22]. The only exception was the $\boldsymbol{b}_3$ ion, which was observed from species **A** to **F**, and was previously determined to form an oxazolone structure [58, 59]. The formation of the $\boldsymbol{y}_4$ ion which was also observed from **A** to **F** was consistent with the Pro effect [51] which enhances preference for cleavage of the amide bond on the N-terminus side of the Pro residue.

The breakdown curves (Figure 3) of the **A** to **G** precursor ions as a function of lab-frame CE show the primary products, which appeared at the lowest CE; dissociated into secondary products, which appeared at higher CE; and dissociated into the tertiary products, which appeared at the highest CE. The identity of the product ions in each group are shown in Tables S1 and S2. Comparison of the CE where the $[amb_5 + H]^+$ of **A** to **G** was 50% dissociated into products (Figure 3, Table 2) shows a general trend related to size and the number of vibrational modes available to absorb the CE. For example, **A** and **B** whose mass only differed by 1 Da exhibited the same 47.1 V_{lab} breakdown energy and a similar pattern for the formation of the primary, secondary, and tertiary products.

To correct for inelastic collisions, where the initial lab-frame energy is converted into translational, rotational, or vibrational energy, the CE was converted to center-of-mass CE, $E_{cm} = CE\ M_{Ar}/(M_{Ar} + M_{amb})$ where M_{Ar} is mass of the Ar collision gas and M_{amb} is mass of the amb_5 peptide (Table 2). Collision theory predicted that the $amb_{5A\text{-}G}$ precursors undergo ~600–700 collisions as they pass through the transfer cell. The $[amb_5 + H]^+$ of **A**, **B**, **E**, and **F** exhibited the highest breakdown energies, $E_{cm} = 2.09$ to 2.10 eV, which coincided with their lowest energy B3LYP conformers (Figures 1c, S1, and S3) containing the imidazolium of His_6 hydrogen bonded to two backbone carbonyl groups, and salt-bridges or hydrogen bonds from the His_1 or Tyr_5 substituent groups to the C-terminus (Table 2). Species **C**, **D**, and **G** exhibited the lowest breakdown energies, $E_{cm} = 1.02$ to 1.89 eV, because the replacement of the His residues with either Gly or Cys removed these salt-bridge or hydrogen-bonding interactions.

The principal CID products of the negatively charged $[amb_5 - H]^-$ (Figure S7c, Table S2) for **A**, **C**, and **D** were the loss of H_2S, $2H_2S$, $2H_2S + CO_2$ and the formation of the $\boldsymbol{z}_6 - 2H_2S$ ion. The $H_2S + CO_2$ loss channel is favored when Cys is the C-terminal residue as previously observed from the Gly-Cys dipeptide [47, 49]. Species **B** did not exhibit $2H_2S + CO_2$ loss, because CO_2 loss could not form from the amidated C-terminus. Species **E** and **F** exhibited CO_2 loss and formation of $\boldsymbol{c}_4$ and $\boldsymbol{c}_1$ ions that were only observed after the thiol of Cys_2 was removed from the primary structure. Previous CID studies of negative ion peptides have also reported the common occurrence of ***c*** ions [37, 75].

The breakdown curves of the $[amb_5 - H]^-$ (Figure 3) of **A** and **C** were similar and exhibited the same $E_{cm} = 1.82$ eV breakdown energy. However, species **B** and **G** exhibited much lower breakdown energies of $E_{cm} = 1.26$ eV and 1.23 eV, respectively, with **B** showing exclusive H_2S and $2H_2S$ loss, while **G** also showed these channels with a range of secondary and tertiary products (Table S2). These observations indicated the amidation of the C-terminus made H_2S and $2H_2S$ loss more labile. Previous work at the HF/6-31G(d)//AM1 level of theory showed H_2S loss was initiated by formation of an enolate anion on the peptide backbone and passage over 0.87 eV transition state barrier followed by stepwise elimination of HS^- and proton transfer [47]. However, when Cys was the C-terminus residue, $H_2S + CO_2$ loss was the prominent channel which occurred through a carboxylate charge-directed mechanism with a higher transition state barrier of 2.9 eV [47]. The amidation of the C-terminus, therefore, restricts the charge-directed mechanism and allows the H_2S loss to proceed over the lower energy barrier. The amidation of the C-terminus also meant the salt-bridge between His_1 and the carboxylate of the C-terminus, exhibited by the 1- conformers of **A** (Figure 2c) and **C** (Figure S5b) changed to a hydrogen bond for conformer **B** (Figure S5a). The His_1 and the salt-bridge were also removed in **D** which exhibited a similarly low $E_{cm} = 1.58$ eV breakdown energy. However, the 1- conformers of **E** and **F** had the highest breakdown energies of $E_{cm} = 1.87$ eV and 2.47 eV, respectively, because **E** produced $H_2S + CO_2$ loss which had to pass over the high transition state barrier, and the thiol-free primary structure of **F** did not exhibit the labile H_2S loss.

Zn(II)-Binding and Charge Distributions Between pH 5 and 10

How changes in the primary structure of **A** affected the Zn(II) chelation was tested by the IM-MS analyses of equimolar mixtures of either **A** to **G** with Zn(II) as a function of pH. Samples of the mass spectra for negative and positive ion species are shown in Figure 4. The main observed species included both singly and doubly charged $amb_{5A\text{-}G}$ and

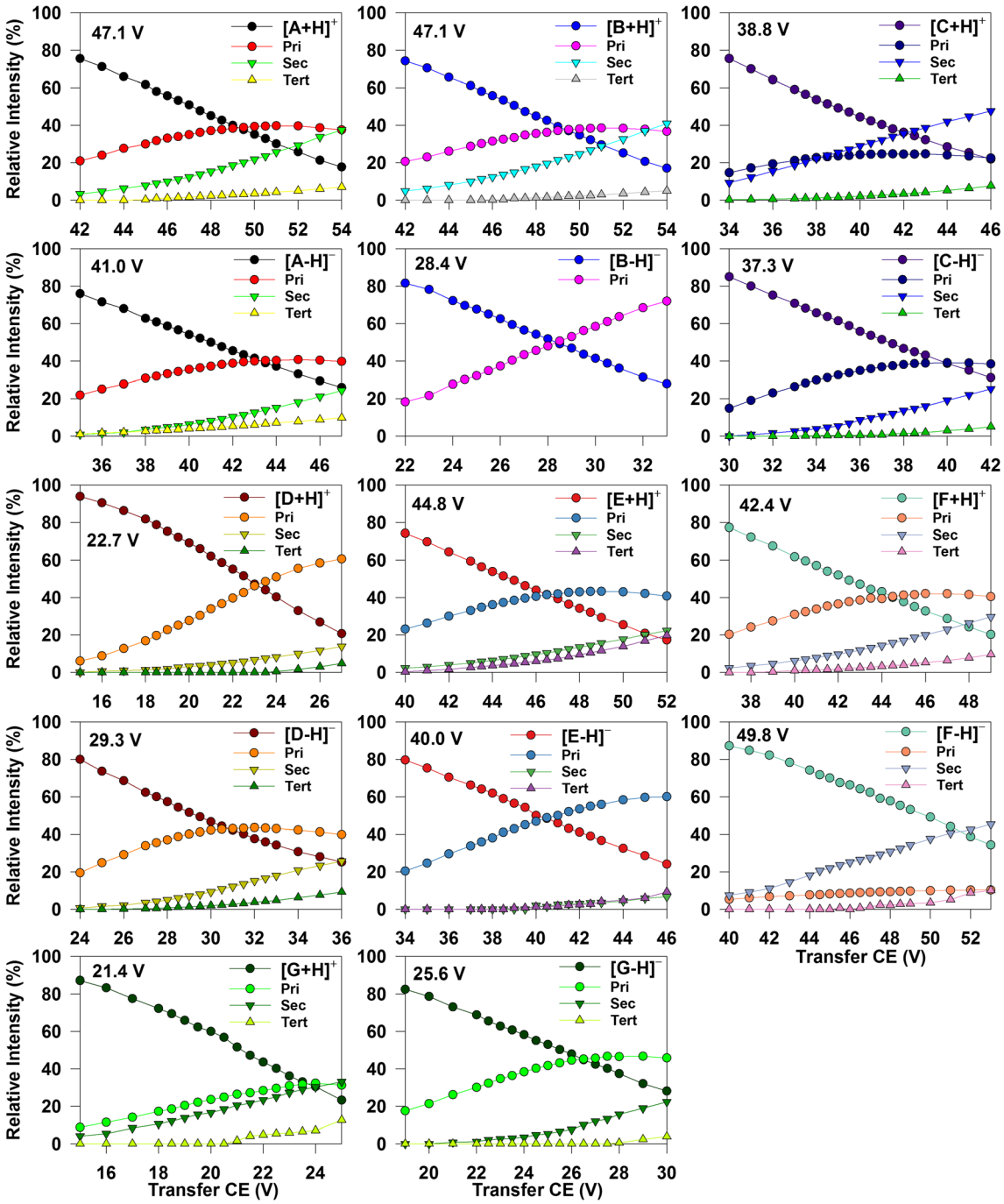

Figure 3. Energy-resolved CID of the negatively and positively charged precursor **A** to **G** with products (Tables S1 and S2) grouped into the primary (Pri), secondary (Sec), and tertiary (Tert) products as described in the text. The lab-frame transfer collision energy where the **A** to **G** precursor was 50% dissociated into products is also shown

$amb_{5A\text{-}G}$ + Zn(II). The overall charge of the species was conserved by the loss or gain of protons, i.e., $[amb_5 - H]^-$, $[amb_5 - 2H]^{2-}$, $[amb_5 - 3H + Zn(II)]^-$, $[amb_5 + 2H]^{2+}$, $[amb_5 - H + Zn(II)]^+$, etc. Lesser signal for chloride adducts were observed, i.e., $[amb_5 - 2H + Zn(II) + Cl]^-$, and some dimers and trimers, i.e., $[triamb_5 - 7H + 3Zn(II)]^-$. A principal species was $[amb_5 - 3H + Zn(II)]^-$ relating to the loss of 3 protons from the 2Cys and C-terminus which were the potentially important Zn(II)-chelating sites.

Distributions of Negatively Charged Species from $amb_{5A\text{-}G}$ + Zn(II) over pH 5 to pH 10

The analyses of negative ions (Figure 5) shows that all species **A** to **G** were principally in the $[amb_5 - H]^-$ form at pH 5 or 6, but as pH increased to pH 7 and higher, the relative intensity of $[amb_5 - 3H + Zn(II)]^-$ increased and became the principal species, apart from species **F**. Previous research of **A** and **B** indicated that the most favorable Zn(II) chelation was via the

Table 2. Breakdown Energies for Positive and Negative Ions of the amb_{5A-G} Measured by Ion Mobility–Mass Spectrometry, Converted from the Lab-Frame (CE) to the Center-of-Mass Frame (E_{cm}) with the Number of Collisions Each Species Undergoes in the Transfer T-Wave Cell, and C-Terminus Interactions

	$[amb_5 + H]^+$				$[amb_5\text{-}H]^-$			
	CE (V)[1]	E_{cm} (eV)[2]	Col[3]	C-term[4]	CE (V)[1]	E_{cm} (eV)[2]	Col[3]	C-term[4]
A	47.1	2.09	685	His_1-SB, Tyr_5-HB	41.0	1.82	675	His_1-SB, Tyr_5-HB
B	47.1	2.10	692	His_1-HB, Tyr_5-HB	28.4	1.26	692	His_1-HB, Tyr_5-HB
C	38.8	1.89	654	His_1-HB	37.3	1.82	627	His_1-SB, Tyr_5-HB
D	22.7	1.23	596	Tyr_5-HB	29.3	1.58	579	–
E	44.8	2.10	661	His_1-SB, Tyr_5-HB	40.0	1.87	651	His_1-HB, Tyr_5-HB
F	42.4	2.10	640	His_1-SB, Tyr_5-HB	49.8	2.47	616	His_1-HB, Tyr_5-HB
G	21.2	1.02	651	Tyr_5-HB	25.6	1.23	723	Tyr_5-HB

[1]Lab-frame collision energy associated with the 50% breakdown of the precursor ion
[2]Center-of-mass collision energy associated with the 50% breakdown of the precursor ion
[3]Number of collisions the amb_5 species undergoes in the transfer T-wave cell calculated by $1.41\ \pi\ \Omega_{amb}(P/kT)d$, where Ω_{amb} are the CCS from Table 1 converted to m^2, $P = 3.2$ Pa, and $d = 0.100$ m is the length of the T-wave cell
[4]Salt-bridge (SB) or hydrogen bond (HB) interactions from His_1 or Tyr_5 to the C-terminus observed in the lowest energy B3LYP conformer

2His-2Cys, C-terminus, and backbone carbonyl oxygen [14]. Figure 5 shows that species **A**, **B**, and **C** were predominantly in the $[amb_5 - 3H + Zn(II)]^-$ form by pH 7, even though **B** had the blocked C-terminus which excluded Zn(II) chelation by the deprotonated carboxylate group, and **C** had His_6 replaced by Gly_6. Species **D** and **E** also exhibited formation of $[amb_5 - 3H + Zn(II)]^-$ as the major species at pH 9–10 showing Zn(II) chelation was still favorable at this pH when neither imidazole or the thiol of Cys_2 were present in the primary structure. Species **D** gave only trace formation of $[amb_5 - 4H + Zn(II)]^{2-}$, indicating that the basic properties of His which were present in **A**, **B**, **C**, and **E** enhanced these latter species deprotonation. Species **F** mainly formed $[amb_5 - H]^-$ over pH 5–10 and exhibited < 12% of $[amb_5 - 3H + Zn(II)]^-$ and $[amb_5 - 4H + Zn(II)]^{2-}$ at any pH which showed that Zn(II) chelation was most dependent on the availability of at least one thiolate site. However, species **G** which had 4Cys in its primary structure was less effective at chelating Zn(II) than **A**, **B**, and **C** which all had His_1 with the 2Cys in their primary structure over pH 7–8.

Distributions of Positively Charged Species from amb_{5A-G} + Zn(II) over pH 5 to pH 10

A similar pH-dependent behavior to the negative ions was observed for positive ions (Figure S8) with **A** to **G** predominantly forming either $[amb_5 + 2H]^{2+}$ and/or $[amb_5 + H]^+$ at pH 5–6 and as pH increased the formation of $[amb_5 - H + Zn(II)]^+$ and $[amb_5 + Zn(II)]^{2+}$ became more significant. This

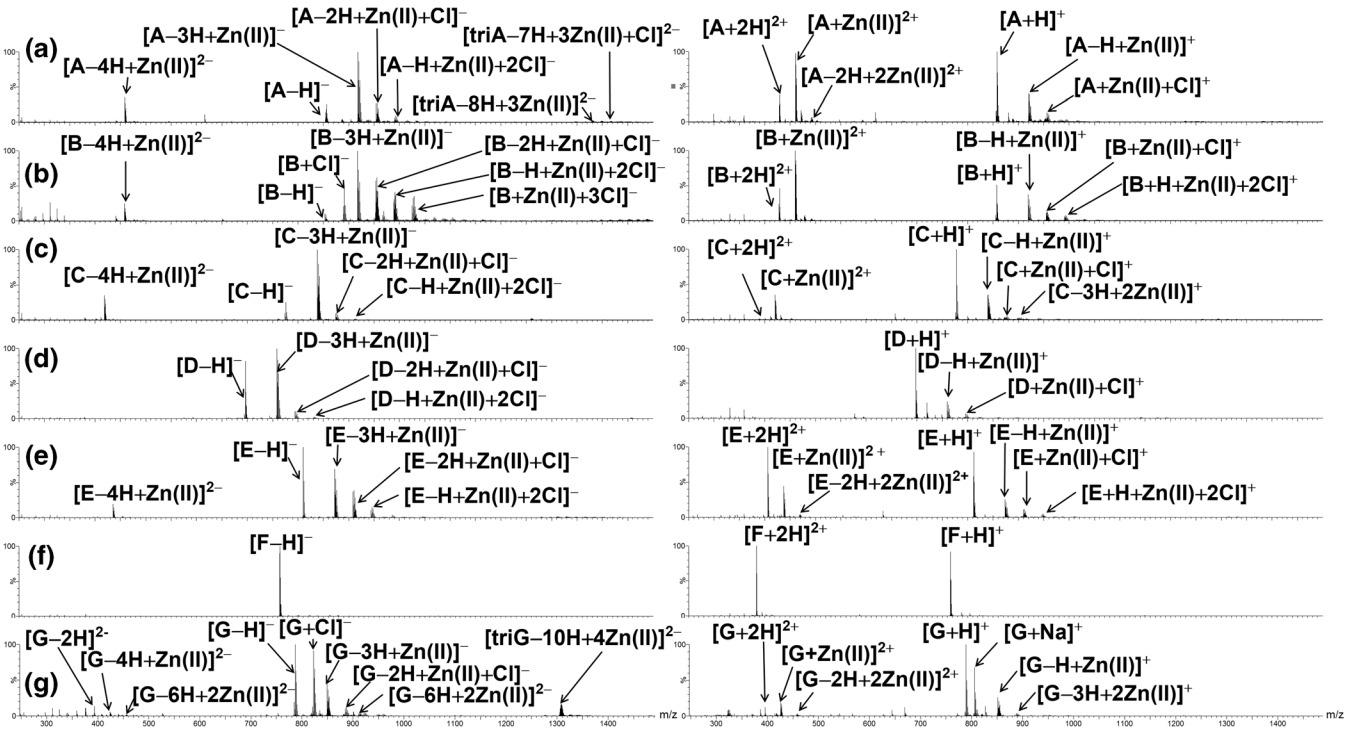

Figure 4. Labeled mass spectra of the products observed from the reactions of (**a**) amb_{5A}, (**b**) amb_{5B}, (**c**) amb_{5C}, (**d**) amb_{5D}, (**e**) amb_{5E}, (**f**) amb_{5F}, or (**g**) amb_{5G} with equimolar $ZnCl_2$ at pH 9. Left panel: negative ions. Right panel: positive ions

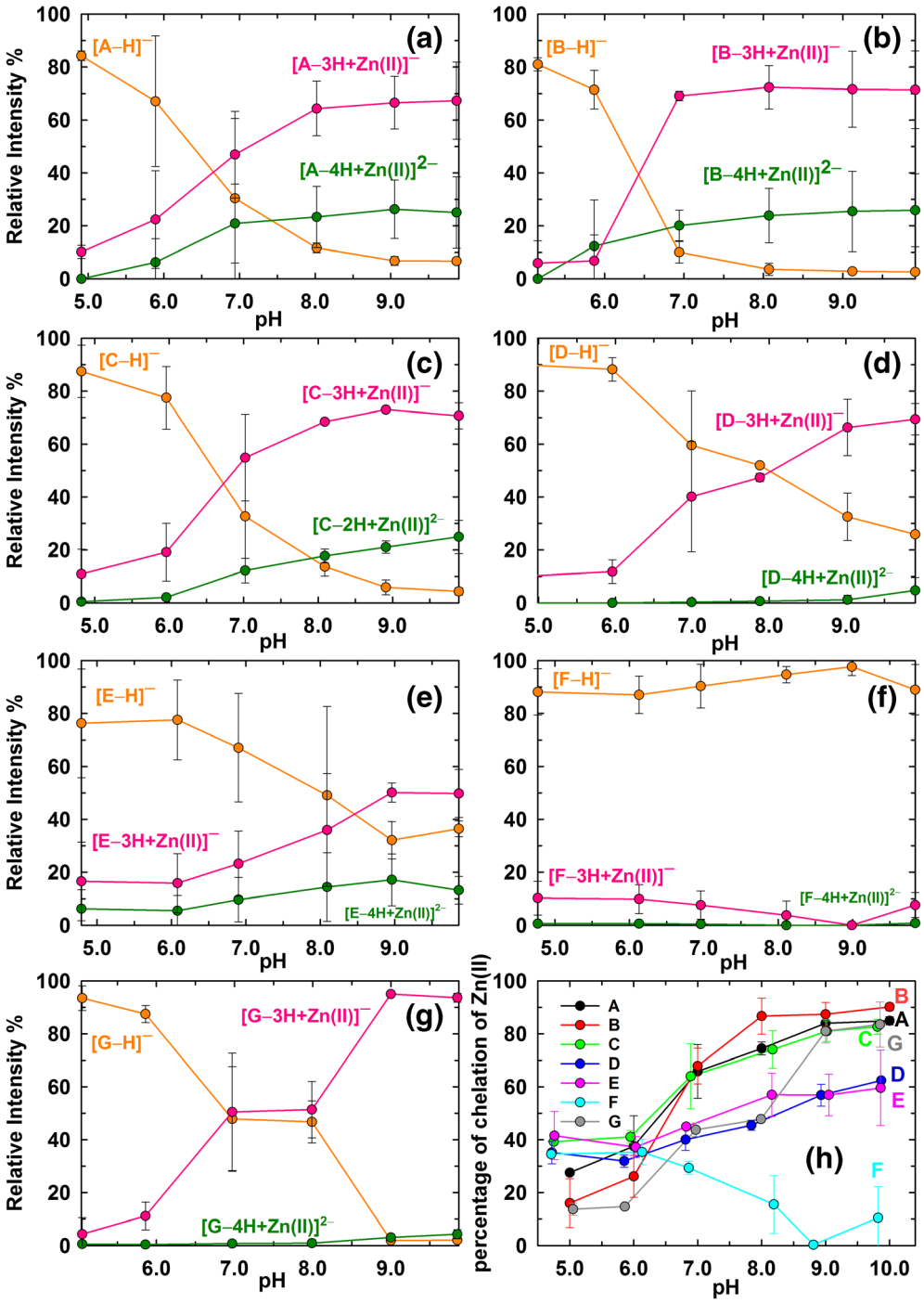

Figure 5. Percent relative intensities of $[amb_5 - H]^-$, $[amb_5 - 3H + Zn(II)]^-$, and $[amb_5 - 4H + Zn(II)]^{2-}$ measured from equimolar mixtures of Zn(II) and either (**a**) amb_{5A}, (**b**) amb_{5B}, (**c**) amb_{5C}, (**d**) amb_{5D}, (**e**) amb_{5E}, (**f**) amb_{5F}, or (**g**) amb_{5G} over the range pH 5–10, and (**h**) the total percentage of all positively and negatively charged Zn(II)-bound species observed from these equimolar mixtures. The error bars are one standard deviation about the mean

indicated that the weakly basic and acidic substituent groups of His and Cys were playing a key role in chelation for the positive ions, because other possible chelating groups such as the backbone carbonyl oxygens or the carboxyl of the C-terminus would not exhibit this pH dependence. For the overall 2+ charge of **A**, $[amb_{5A} + Zn(II)]^{2+}$, the B3LYP modeling predicted the lowest energy Zn(II) coordination was via the two thiolates of the 2Cys, with 2His protonated as imidazoliums (Figure S9). Other options such as the imidazole coordination of Zn(II) and the Cys protonated as thiols were higher in energy and indicated that Cys could not chelate Zn(II) via the protonated thiol groups. Species **A**, **B**, **C**, **D**, **E**, and **G** exhibited increases of $[amb_5 - H + Zn(II)]^+$ and $[amb_5 + Zn(II)]^{2+}$ over pH 5–10, with the exceptions of **D** and **G** which

did not form or formed < 10% of $[amb_5 + Zn(II)]^{2+}$, which coincided with their primary structures not containing His. Species **F** was the only species that exhibited a decrease in the formation of $[amb_5 - H + Zn(II)]^{+}$ and $[amb_5 + Zn(II)]^{2+}$ over pH 5–10, even though its sequence contained two imidazoles that were potential Zn(II) chelation sites.

Comparative Zn(II) Chelation by $amb_{5A\text{-}G}$ from Both Positive and Negative Ion Analyses

To determine the overall effectiveness of **A** to **G** for Zn(II) chelation, a plot that includes the relative percentages of all Zn(II)-bound species from the positive and negative charge analyses are shown in Figure 5h. At pH 5 and 6, all species exhibited ~15–40% Zn(II) chelation with the species with the amidated C-terminus, **B** and **G**, exhibiting the lowest binding, indicating the C-terminus carboxylate was involved in chelating Zn(II). As pH increased (pH ≥ 7) **A**, **B**, and **C** exhibited the greatest percent increase of Zn(II) chelation, with 65–92% of species chelating Zn(II). The modifications to the primary structure of **A** by substituting 2His with 2Gly (**D**) and Cys_2 with Gly_2 (**E**) decreased the percent of Zn(II) chelation to 38–62% over pH 7 to 10, whereas substituting 2Cys with 2Gly (**F**) further decreased Zn(II) chelation from 35 to 10% over pH 5 to 10. The substitution of 2His with 2Cys (**G**) also lowered Zn(II) chelation to ~45% over pH 7–8, compared to 70–90% for **A**, **B**, and **C**, indicating that the weak base property of His was required for efficient Zn(II) chelation over this pH range. Only at pH 9–10 was Zn(II) chelation exhibited by **G** equivalent to that exhibited by **A**, **B**, and **C**. This pH-dependent behavior showed that the amb_5 peptides containing His_1 and 2Cys exhibited the most effective Zn(II) chelation and provided evidence for the His role as proton acceptor for the deprotonation of Cys which acts as the most favorable Zn(II)

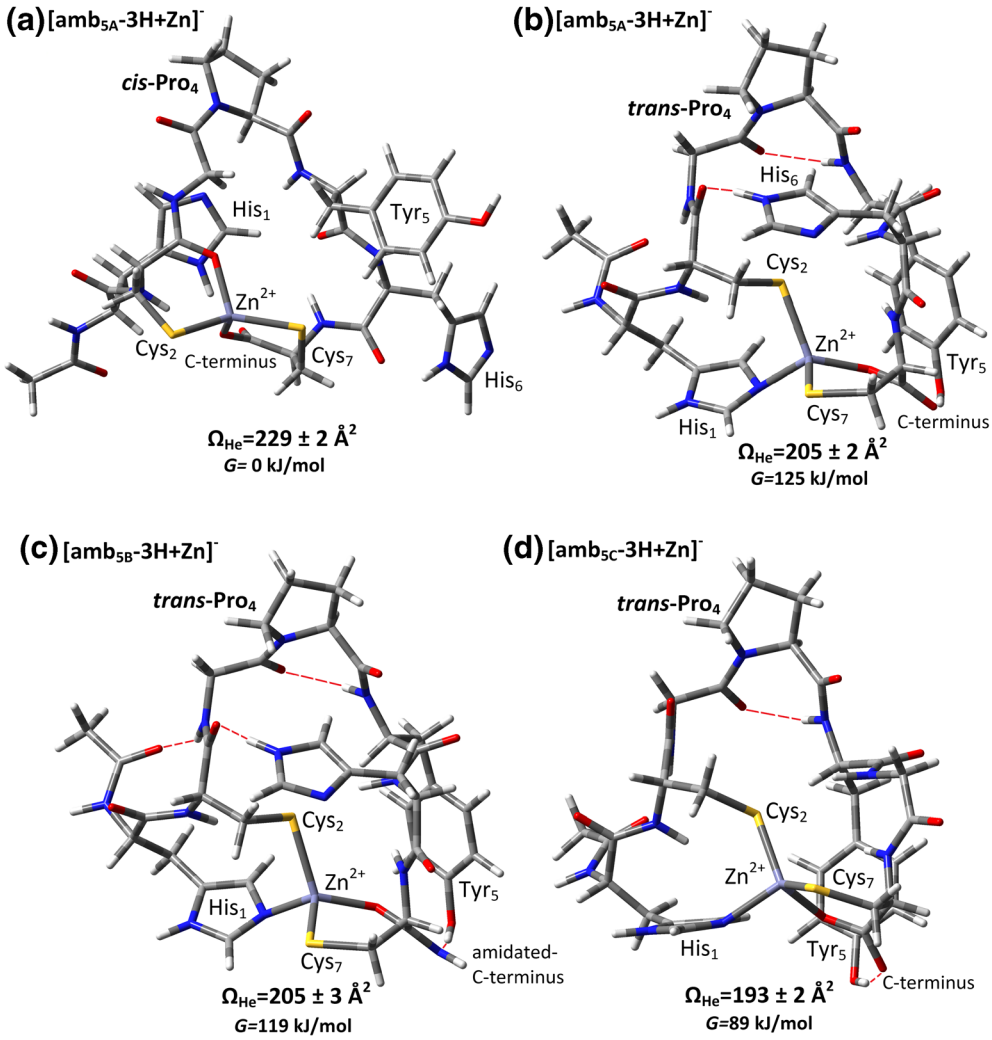

Figure 6. Comparison of the conformers located using the B3LYP/LanL2DZ method (**a**) *cis*-Pro $[amb_{5A} - 3H + Zn]^-$ exhibiting 2Cys, backbone carbonyl and C-terminus coordination of Zn(II), (**b**) *trans*-Pro $[amb_{5A} - 3H + Zn]^-$ exhibiting His_1-2Cys and C-terminus coordination of Zn(II), **(c)** *trans*-Pro $[amb_{5B} - 3H + Zn]^-$ exhibiting His_1-2Cys and the amidated C-terminus coordination of Zn(II), and (**d**) *trans*-Pro $[amb_{5C} - 3H + Zn]^-$ exhibiting His_1-2Cys and C-terminus coordination of Zn(II), with the relative free energies (*G*), theoretical collision cross sections (Ω_{He}), [74] and hydrogen bonds (---) shown

anchoring site at pH 7–10. The two imidazoles did not effectively chelate Zn(II) at pH > 7 as evidenced by species **F** which exhibited the lowest Zn(II) chelation because its primary structure did not contain the two thiol groups. As pH becomes more basic, competition from the formation of $Zn(OH)_2$ may necessitate that thiolate ligands are present in the amb_5 sequence for effective Zn(II) chelation.

Collision Cross Sections and Zn(II) Coordination Exhibited by Positive and Negative Ions

A series of geometry-optimized conformers were located using the B3LYP/LanL2DZ method for $[amb_5 - 3H + Zn]^-$ (Figure 6). The lowest free energy conformer of **A** contained *cis*-Pro (Figure 6a), which is the same *cis*-Pro conformer reported in our previous paper [14] but optimized with the acetylated N-terminal arm in the *trans*-configuration that lowered the free energy by 3.3 kJ/mol. The conformer exhibits Zn(II) chelation via 2Cys, carbonyl O of Cys_2, and the carboxylate of the C-terminus. However, the LJ CCS of conformer **6a**, $\Omega_{He} = 229 \pm 2$ Å^2, is significantly larger than the IM-MS measured $\Omega_{He} = 200 \pm 4$ Å^2 (Table 1) and this disparity was reported in our previous paper [14]. In our present research, a new series of *trans*-conformers were located and the lowest free energy *trans*-Pro conformer (Figure 6b) exhibited His_1-Cys_2-Cys_7 and carboxylate C-terminus Zn(II) coordination with $\Omega_{He} = 205 \pm 2$ Å^2, in much better agreement with the IM-MS $\Omega_{He} = 200 \pm 4$ Å^2. Previous research [6, 77] has shown that IM-MS analyses can distinguish between the *cis*- and *trans*-Pro conformers of oligopeptides. The B3LYP/LanL2DZ method predicts that the *trans*-Pro conformer **6b** is 125 kJ/mol higher in free energy than the *cis*-Pro conformer **6a**. However, all the peptides **A** to **G** were originally synthesized with *trans*-peptide bonds and so the energy barrier for conversion of *trans*-Pro_4 to *cis*-Pro may restrict its formation. This is further supported by the Ω_{He} of the *trans*-Pro conformers of **B** (Figure 6c) and **C** (Figure 6d) which also exhibit Ω_{He} in agreement with the IMMS measured Ω_{He} (Table 1), whereas their *cis*-Pro conformers were significantly larger (Figure S10). The *trans*-Pro conformers with their preference for His_1-Cys_2-Cys_7 and C-terminus Zn(II) coordination also explains why **A**, **B**, and **C** are the most effective Zn(II) chelators because they contain all these chelating groups, whereas the Zn(II)-chelating ability of **D**, **E**, **F**, and **G** were all adversely affected when one or two of these chelating sites were modified.

Conclusions

Using IM-MS and B3LYP/LanL2DZ computational studies, we have investigated the oligopeptide acetyl-His_1-Cys_2-Gly_3-Pro_4-Tyr_5-His_6-Cys_7 which contained the 2His-2Cys motif and a series of oligopeptides that have modifications to the potential His, Cys, or C-terminus Zn(II)-binding sites. The results show that at pH ≥ 7, the weak basic properties of His are intrinsically linked to the weak acid properties of Cys through a proton transfer reaction which affects the charge states, tertiary structures, and Zn(II) coordination of the oligopeptides studied here. The positive and negative charge states were primarily influenced by the imidazolium groups and their interactions with the thiolates and carboxylate of the C-terminal. The lowest free energy B3LYP conformers predicted a salt-bridged interaction between the imidazolium and C-terminus carboxylate and the deprotonation of the thiols by the imidazoles acting as proton acceptors and providing electrostatic stabilization of the thiolates via salt-bridging or hydrogen bonding. These acid-base interactions of His and Cys also lowered the pH at which Zn(II) chelation effectively occurred, indicating that imidazoles act as proton acceptors for the deprotonation of the thiol groups that are the primary anchoring sites for Zn(II). This was supported by the DFT conformers which contained *trans*-Pro and His_1-Cys_2-Cys_7 and C-terminus Zn(II) coordination whose theoretical Ω_{He} were in good agreement with the IM-MS measured Ω_{He}.

Acknowledgements

This material is based upon work supported by the National Science Foundation under, NSF instrument support (MRI-0821247), Welch Foundation (T-0014), and computing resources from the Department of Energy (TX-W-20090427-0004-50) and L3 Communications. We thank the Bower's group of University of California – Santa Barbara for sharing the Sigma program.

References

1. Choutko, A., van Gunsteren, W.F.: Conformational preferences of a beta-octapeptide as function of solvent and force-field parameters. Helv. Chim. Acta. **96**, 189–200 (2013)
2. Lillo, V., Galan-Mascaros, J.R.: Transition metal complexes with oligopeptides: single crystals and crystal structures. Dalton Trans. **43**, 9821–9833 (2014)
3. Berezovskaya, Y., Porrini, M., Nortcliffe, C., Barran, P.E.: The use of ion mobility mass spectrometry to assist protein design: a case study on zinc finger fold versus coiled coil interactions. Analyst. **140**, 2847–2856 (2015)
4. Wyttenbach, T., Liu, D., Bowers, M.T.: Interactions of the hormone oxytocin with divalent metal ions. J. Am. Chem. Soc. **130**, 5993–6000 (2008)
5. Sitkiewicz, E., Kloniecki, M., Poznanski, J., Bal, W., Dadlez, M.: Factors influencing compact-extended structure equilibrium in oligomers of Aβ1-40 peptide - an ion mobility mass spectrometry study. J. Mol. Biol. **426**, 2871–2885 (2014)
6. Fuller, D.R., Glover, M.S., Pierson, N.A., Clemmer, D.E., Kim, D., Russell, D.H.: Cis→trans isomerization of pro(7) in oxytocin regulates Zn(2+) binding. J. Am. Soc. Mass Spectrom. **27**, 1376–1382 (2016)
7. Glover, M.S., Dilger, J.M., Zhu, F., Clemmer, D.E.: The binding of Ca2+, Co2+, Ni2+, Cu2+, and Zn2+ cations to angiotensin I determined by mass spectrometry based techniques. Int. J. Mass Spectrom. **354-355**, 318–325 (2013)
8. Vytla, Y., Angel, L.A.: Applying ion mobility-mass spectrometry techniques for explicitly identifying the products of Cu(II) reactions of 2His-2Cys motif peptides. Anal. Chem. (Washington, DC, U. S.). **88**, 10925–10932 (2016)
9. Martin, E.M., Kondrat, F.D.L., Stewart, A.J., Scrivens, J.H., Sadler, P.J., Blindauer, C.A.: Native electrospray mass spectrometry approaches to probe the interaction between zinc and an anti-angiogenic peptide from histidine-rich glycoprotein. Sci. Rep. **8**, 1–13 (2018)

10. Choi, D.W., Sesham, R., Kim, Y., Angel, L.A.: Analysis of methanobactin from Methylosinus trichosporium OB3b via ion mobility mass spectrometry. Eur. J. Mass Spectrom. **18**, 509–520 (2012)
11. McCabe, J.W., Vangala, R., Angel, L.A.: Binding selectivity of methanobactin from Methylosinus trichosporium OB3b for copper(I), silver(I), zinc(II), nickel(II), cobalt(II), manganese(II), lead(II), and iron(II). J. Am. Soc. Mass Spectrom. **28**, 2588–2601 (2017)
12. Sesham, R., Choi, D., Balaji, A., Cheruku, S., Ravichetti, C., Alshahrani, A.A., Nasani, M., Angel, L.A.: The pH dependent Cu(II) and Zn(II) binding behavior of an analog methanobactin peptide. Eur. J. Mass Spectrom. **19**, 463–473 (2013)
13. Choi, D., Alshahrani, A.A., Vytla, Y., Deeconda, M., Serna, V.J., Saenz, R.F., Angel, L.A.: Redox activity and multiple copper(I) coordination of 2His-2Cys oligopeptide. J. Mass Spectrom. **50**, 316–325 (2015)
14. Wagoner, S.M., Deeconda, M., Cumpian, K.L., Ortiz, R., Chinthala, S., Angel, L.A.: The multiple conformational charge states of zinc(II) coordination by 2His-2Cys oligopeptide investigated by ion mobility - mass spectrometry, density functional theory and theoretical collision cross sections. J. Mass Spectrom. **51**, 1120–1129 (2016)
15. El Ghazouani, A., Basle, A., Firbank, S.J., Knapp, C.W., Gray, J., Graham, D.W., Dennison, C.: Copper-binding properties and structures of methanobactins from Methylosinus trichosporium OB3b. Inorg. Chem. **50**, 1378–1391 (2011)
16. Balasubramanian, R., Kenney, G.E., Rosenzweig, A.C.: Dual pathways for copper uptake by methanotrophic bacteria. J. Biol. Chem. **286**, 37313–37319 (2011)
17. Balasubramanian, R., Rosenzweig, A.C.: Copper methanobactin: a molecule whose time has come. Curr. Opin. Chem. Biol. **12**, 245–249 (2008)
18. Behling, L.A., Hartsel, S.C., Lewis, D.E., DiSpirito, A.A., Choi, D.W., Masterson, L.R., Veglia, G., Gallagher, W.H.: NMR, mass spectrometry and chemical evidence reveal a different chemical structure for methanobactin that contains oxazolone rings. J. Am. Chem. Soc. **130**, 12604–12605 (2008)
19. Kim, H.J., Graham, D.W., DiSpirito, A.A., Alterman, M.A., Galeva, N., Larive, C.K., Asunskis, D., Sherwood, P.M.: Methanobactin, a copper-acquisition compound from methane-oxidizing bacteria. Science. **305**, 1612–1615 (2004)
20. Klug, A.: The discovery of zinc fingers and their development for practical applications in gene regulation and genome manipulation. Q. Rev. Biophys. **43**, 1–21 (2010)
21. Harrison, A.G.: The gas-phase basicities and proton affinities of amino acids and peptides. Mass Spectrom. Rev. **16**, 201–217 (1997)
22. Schnier, P.D., Gross, D.S., Williams, E.R.: On the maximum charge state and proton transfer reactivity of peptide and protein ions formed by electrospray ionization. J. Am. Soc. Mass Spectrom. **6**, 1086–1097 (1995)
23. Ewing, N.P., Zhang, X., Cassady, C.J.: Determination of the gas-phase basicities of proline and its di- and tripeptides with glycine: the enhanced basicity of prolylproline. J. Mass Spectrom. **31**, 1345–1350 (1996)
24. Stover, M.L., Jackson, V.E., Matus, M.H., Adams, M.A., Cassady, C.J., Dixon, D.A.: Fundamental thermochemical properties of amino acids: gas-phase and aqueous acidities and gas-phase heats of formation. J. Phys. Chem. B. **116**, 2905–2916 (2012)
25. Gross, D.S., Rodriguez-Cruz, S.E., Bock, S., Williams, E.R.: Measurement of coulomb energy and dielectric polarizability of gas-phase diprotonated diaminoalkanes. J. Phys. Chem. **99**, 4034–4038 (1995)
26. Kaltashov, I.A., Fabris, D., Fenselau, C.C.: Assessment of gas phase basicities of protonated peptides by the kinetic method. J. Phys. Chem. **99**, 10046–10051 (1995)
27. Kaltashova, I.A., Fenselau, C.: Thermochemistry of multiply charged melittin in the gas phase determined by the modified kinetic method. Rapid Commun. Mass Spectrom. **10**, 857–861 (1996)
28. Nielsen, B.V., Abaye, D.A.: Influence of electrolytes and a supercharging reagent on charge state distribution and response of neuropeptide ions generated during positive electrospray ionisation mass spectrometry. Eur. J. Mass Spectrom. (Chichester, Eng). **19**, 335–344 (2013)
29. Metwally, H., Duez, Q., Konermann, L.: Chain ejection model for electrospray ionization of unfolded proteins: evidence from atomistic simulations and ion mobility spectrometry. Anal. Chem. (Washington, DC, U. S.). **90**, 10069–10077 (2018)
30. Wang, G., Cole, R.B.: Disparity between solution-phase equilibria and charge state distributions in positive-ion electrospray mass spectrometry. Org. Mass Spectrom. **29**, 419–427 (1994)
31. Oda, Y., Yamazaki, T., Nagayama, K., Kanaya, S., Kuroda, Y., Nakamura, H.: Individual ionization constants of all the carboxyl groups in ribonuclease HI from Escherichia coli determined by NMR. Biochemistry. **33**, 5275–5284 (1994)
32. Elferich, J., Williamson, D.M., David, L.L., Shinde, U.: Determination of histidine pKa values in the propeptides of furin and proprotein convertase 1/3 using histidine hydrogen-deuterium exchange mass spectrometry. Anal. Chem. (Washington, DC, U. S.). **87**, 7909–7917 (2015)
33. Miyagi, M., Nakazawa, T.: Determination of pKa values of individual histidine residues in proteins using mass spectrometry. Anal. Chem. **80**, 6481–6487 (2008)
34. Madzelan, P., Labunska, T., Wilson, M.A.: Influence of peptide dipoles and hydrogen bonds on reactive cysteine pKa values in fission yeast DJ-1. FEBS J. **279**, 4111–4120 (2012)
35. Lau, K.W., Hart, S.R., Lynch, J.A., Wong, S.C.C., Hubbard, S.J., Gaskell, S.J.: Observations on the detection of b- and y-type ions in the collisionally activated decomposition spectra of protonated peptides. Rapid Commun. Mass Spectrom. **23**, 1508–1514 (2009)
36. Zhang, Z.: Prediction of low-energy collision-induced dissociation spectra of peptides. Anal. Chem. **76**, 3908–3922 (2004)
37. Pu, D., Clipston, N.L., Cassady, C.J.: A comparison of positive and negative ion collision-induced dissociation for model heptapeptides with one basic residue. J. Mass Spectrom. **45**, 297–305 (2010)
38. Harrison, A.G., Tasoglu, C., Yalcin, T.: Non-direct sequence ions in the tandem mass spectrometry of protonated peptide amides-an energy-resolved study. J. Am. Soc. Mass Spectrom. **24**, 1565–1572 (2013)
39. Bokatzian-Johnson, S.S., Stover, M.L., Dixon, D.A., Cassady, C.J.: Gas-phase deprotonation of the peptide backbone for tripeptides and their methyl esters with hydrogen and methyl side chains. J. Phys. Chem. B. **116**, 14844–14858 (2012)
40. Rogalewicz, F., Hoppilliard, Y., Ohanessian, G.: Structures and fragmentations of zinc(II) complexes of amino acids in the gas phase. III. Rearrangement versus desolvation in the electrospray formation of the glycine-zinc complex. Int. J. Mass Spectrom. **206**, 45–52 (2001)
41. Rogalewicz, F., Hoppilliard, Y., Ohanessian, G.: Structures and fragmentations of zinc(II) complexes of amino acids in the gas phase - IV. Solvent effect on the structure of electrosprayed ions. Int. J. Mass Spectrom. **227**, 439–451 (2003)
42. Hoppilliard, Y., Rogalewicz, F., Ohanessian, G.: Structures and fragmentations of zinc(II) complexes of amino acids in the gas phase. II. Decompositions of glycine-Zn(II) complexes. Int. J. Mass Spectrom. **204**, 267–280 (2001)
43. Watson, H.M., Vincent, J.B., Cassady, C.J.: Effects of transition metal ion coordination on the collision-induced dissociation of polyalanines. J. Mass Spectrom. **46**, 1099–1107 (2011)
44. Giganti, V.G., Kundoor, S., Best, W.A., Angel, L.A.: Ion mobility-mass spectrometry study of folded ubiquitin conformers induced by treatment with cis-$Pd(en)(H_2O)_2^{2+}$. J. Am. Soc. Mass Spectrom. **22**, 300–309 (2011)
45. Nelson, C.R., Abutokaikah, M.T., Harrison, A.G., Bythell, B.J.: Proton mobility in b2 ion formation and fragmentation reactions of histidine-containing peptides. J. Am. Soc. Mass Spectrom. **27**, 487–497 (2016)
46. Fu, Q., Li, L.: Neutral loss of water from the b ions with histidine at the C-terminus and formation of the c ions involving lysine side chains. J. Mass Spectrom. **41**, 1600–1607 (2006)
47. Bilusich, D., Brinkworth, C.S., McAnoy, A.M., Bowie, J.H.: The fragmentations of $[M-H]^-$ anions derived from underivatised peptides. The side-chain loss of H_2S from Cys. A joint experimental and theoretical study. Rapid Commun. Mass Spectrom. **17**, 2488–2494 (2003)
48. Bilusich, D., Brinkworth, C.S., Bowie, J.H.: Negative ion mass spectra of Cys-containing peptides. The characteristic Cys γ backbone cleavage: A joint experimental and theoretical study. Rapid Commun. Mass Spectrom. **18**, 544–552 (2004)
49. Waugh, R.J., Bowie, J.H., Gross, M.L.: Collision-induced dissociations of deprotonated peptides. Dipeptides containing methionine or cysteine. Rapid Commun. Mass Spectrom. **7**, 623–625 (1993)
50. Ganguly, H.K., Majumder, B., Chattopadhyay, S., Chakrabarti, P., Basu, G.: Direct evidence for CH···π interaction mediated stabilization of pro-*cis*Pro bond in peptides with pro-pro-aromatic motifs. J. Am. Chem. Soc. **134**, 4661–4669 (2012)
51. Harrison, A.G., Young, A.B.: Fragmentation reactions of deprotonated peptides containing proline. The proline effect. J. Mass Spectrom. **40**, 1173–1186 (2005)
52. Utley, B., Angel, L.A.: Effects of transition metal ion identity and π-cation interactions in metal-bis(peptide) complexes containing phenylalanine. Eur. J. Mass Spectrom. **16**, 631–643 (2010)

53. Harrison, A.G.: Fragmentation reactions of protonated peptides containing phenylalanine: a linear free energy correlation in the fragmentation of H-Gly-Xxx-Phe-OH. Int. J. Mass Spectrom. **217**, 185–193 (2002)
54. Harrison, A.G.: Fragmentation reactions of methionine-containing protonated octapeptides and fragment ions therefrom: an energy-resolved study. J. Am. Soc. Mass Spectrom. **24**, 1555–1564 (2013)
55. Bythell, B.J., Csonka, I.P., Suhai, S., Barofsky, D.F., Paizs, B.: Gas-phase structure and fragmentation pathways of singly protonated peptides with N-terminal arginine. J. Phys. Chem. B. **114**, 15092–15105 (2010)
56. El Aribi, H., Rodriquez, C.F., Almeida, D.R.P., Ling, Y., Mak, W.W.N., Hopkinson, A.C., Siu, K.W.M.: Elucidation of fragmentation mechanisms of protonated peptide ions and their products: a case study on glycylglycylglycine using density functional theory and threshold collision-induced dissociation. J. Am. Chem. Soc. **125**, 9229–9236 (2003)
57. Mookherjee, A., Van Stipdonk, M.J., Armentrout, P.B.: Thermodynamics and reaction mechanisms of decomposition of the simplest protonated tripeptide, triglycine: a guided ion beam and computational study. J. Am. Soc. Mass Spectrom. **28**, 739–757 (2017)
58. Allen, J.M., Racine, A.H., Berman, A.M., Johnson, J.S., Bythell, B.J., Paizs, B., Glish, G.L.: Why are a3 ions rarely observed? J. Am. Soc. Mass Spectrom. **19**, 1764–1770 (2008)
59. Harrison, A.G.: Fragmentation reactions of some peptide b3 ions: an energy-resolved study. Rapid Commun. Mass Spectrom. **23**, 1298–1302 (2009)
60. Chen, X., Yu, L., Steill, J.D., Oomens, J., Polfer, N.C.: Effect of peptide fragment size on the propensity of cyclization in collision-induced dissociation: Oligoglycine b2-b8. J. Am. Chem. Soc. **131**, 18272–18282 (2009)
61. Zhang, Z., Browne, S.J., Vachet, R.W.: Exploring salt bridge structures of gas-phase protein ions using multiple stages of electron transfer and collision induced dissociation. J. Am. Soc. Mass Spectrom. **25**, 604–613 (2014)
62. Bush, M.F., Campuzano, I.D.G., Robinson, C.V.: Ion mobility mass spectrometry of peptide ions: effects of drift gas and calibration strategies. Anal. Chem. **84**, 7124–7130 (2012)
63. Forsythe, J.G., Petrov, A.S., Walker, C.A., Allen, S.J., Pellissier, J.S., Bush, M.F., Hud, N.V., Fernandez, F.M.: Collision cross section calibrants for negative ion mode traveling wave ion mobility-mass spectrometry. Analyst. **14**, 6853–6861 (2015)
64. Pringle, S.D., Giles, K., Wildgoose, J.L., Williams, J.P., Slade, S.E., Thalassinos, K., Bateman, R.H., Bowers, M.T., Scrivens, J.H.: An investigation of the mobility separation of some peptide and protein ions using a new hybrid quadrupole/travelling wave IMS/oa-ToF instrument. Int. J. Mass Spectrom. **261**, 1–12 (2007)
65. Raja, U.K.B., Injeti, S., Culver, T., McCabe, J.W., Angel, L.A.: Probing the stability of insulin oligomers using electrospray ionization ion mobility mass spectrometry. Eur. J. Mass Spectrom. **21**, 759–774 (2015)
66. Allen, S.J., Giles, K., Gilbert, T., Bush, M.F.: Ion mobility mass spectrometry of peptide, protein, and protein complex ions using a radio-frequency confining drift cell. Analyst. **141**, 884–891 (2016)
67. Salbo, R., Bush, M.F., Naver, H., Campuzano, I., Robinson, C.V., Pettersson, I., Jørgensen, T.J.D., Haselmann, K.F.: Traveling-wave ion mobility mass spectrometry of protein complexes: accurate calibrated collision cross-sections of human insulin oligomers. Rapid Commun. Mass Spectrom.: RCM. **26**, 1181 (2012)
68. Smith, D.P., Knapman, T.W., Campuzano, I., Malham, R.W., Berryman, J.T., Radford, S.E., Ashcroft, A.E.: Deciphering drift time measurements from travelling wave ion mobility spectrometry-mass spectrometry studies. Eur. J. Mass Spectrom. **15**, 113–130 (2009)
69. Dunning Jr., T.H., Hay, P.J.: Gaussian basis sets for molecular calculations. Mod. Theor. Chem. **3**, 1–27 (1977)
70. Hay, P.J., Wadt, W.R.: Ab initio effective core potentials for molecular calculations. Potentials for K to Au including the outermost core orbitals. J. Chem. Phys. **82**, 299 (1985)
71. Hay, P.J., Wadt, W.R.: Ab initio effective core potentials for molecular calculations. Potentials for the transition metal atoms Sc to Hg. J. Chem. Phys. **82**, 270 (1985)
72. Wadt, W.R., Hay, P.J.: Ab initio effective core potentials for molecular calculations. Potentials for main group elements Na to Bi. J. Chem. Phys. **82**, 284 (1985)
73. Frisch, M.J., Trucks, G.W., Schlegel, H.B., Scuseria, G.E., Robb, M.A., Cheeseman, J.R., Scalmani, G., Barone, V., Mennucci, B., Petersson, G.A., Nakatsuji, H., Caricato, M., Li, X., Hratchian, H.P., Izmaylov, A.F., Bloino, J., Zheng, G., Sonnenberg, J.L., Hada, M., Ehara, M., Toyota, K., Fukuda, R., Hasegawa, J., Ishida, M., Nakajima, T., Honda, Y., Kitao, O., Nakai, H., Vreven, T., Montgomery, J., J. A, Peralta, J.E., Ogliaro, F., Bearpark, M., Heyd, J.J., Brothers, E., Kudin, K.N., Staroverov, V.N., Kobayashi, R., Normand, J., Raghavachari, K., Rendell, A., Burant, J.C., Iyengar, S.S., Tomasi, J., Cossi, M., Rega, N., Millam, J.M., Klene, M., Knox, J.E., Cross, J.B., Bakken, V., Adamo, C., Jaramillo, J., Gomperts, R., Stratmann, R.E., Yazyev, O., Austin, A.J., Cammi, R., Pomelli, C., Ochterski, J.W., Martin, R.L., Morokuma, K., Zakrzewski, V.G., Voth, G.A., Salvador, P., Dannenberg, J.J., Dapprich, S., Daniels, A.D., Farkas, Ö., Foresman, J.B., Ortiz, J.V., Cioslowski, J., Fox, D.J.: Gaussian 09, Revision C.01. Gaussian Inc, Wallingford CT (2012)
74. Wyttenbach, T., von Helden, G., Batka Jr., J.J., Carlat, D., Bowers, M.T.: Effect of the long-range potential on ion mobility measurements. J. Am. Soc. Mass Spectrom. **8**, 275–282 (1997)
75. Bokatzian, S., Stover, M.L., Dixon, D., Cassady, C.: A comparison of the effects of amide and acid groups at the C-terminus on the collision-induced dissociation of deprotonated peptides. J. Am. Soc. Mass Spectrom. **23**, 1544–1557 (2012)
76. Roepstorff, P.: Proposal for a common nomenclature for sequence ions in mass spectra of peptides. Biomed. Mass Spectrom. **11**, 601 (1984)
77. Fuller, D.R., Conant, C.R., El-Baba, T.J., Brown, C.J., Woodall, D.W., Russell, D.H., Clemmer, D.E.: Conformationally regulated peptide bond cleavage in bradykinin. J. Am. Chem. Soc. **140**, 9357–9360 (2018)